

Star-Shaped Distance Voronoi Diagrams for 3D Metamaterial Design

LOGAN NUMEROW, ETH Zürich, Switzerland

STELIAN COROS, ETH Zürich, Switzerland

BERNHARD THOMASZEWSKI, ETH Zürich, Switzerland

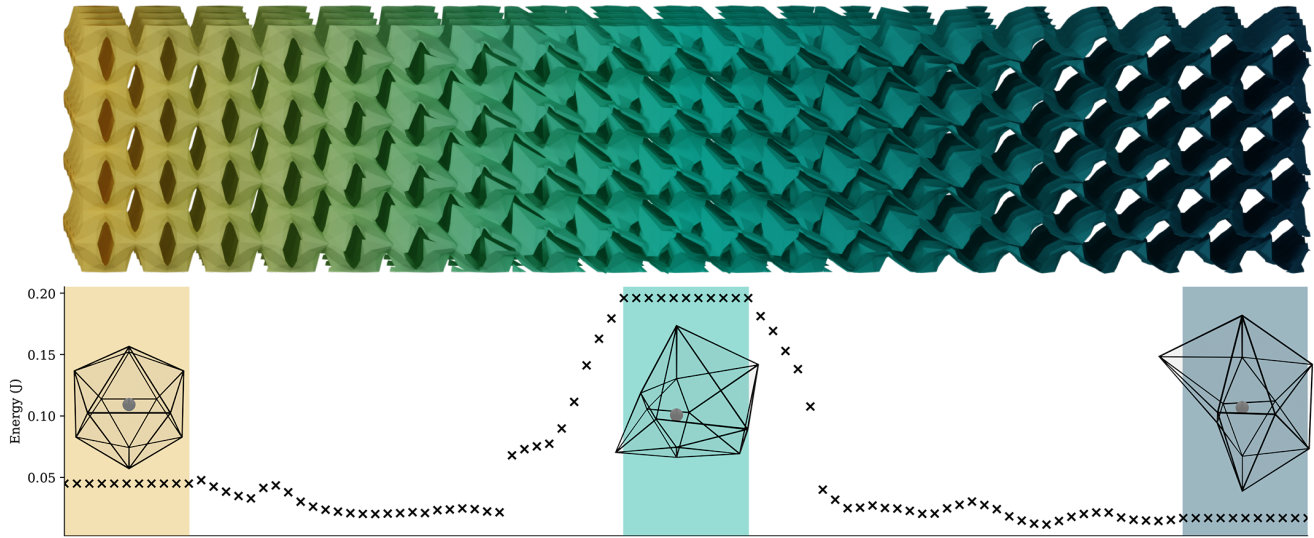


Fig. 1. A graded 3D metamaterial, generated by interpolating parameters of a 3D volumetric star-shaped distance Voronoi diagram. Sites are arranged in a body-centered cubic (BCC) lattice, and Voronoi interfaces are selectively excluded to obtain a porous topology. Metric polyhedra vary along the x -axis, interpolating between the three polyhedra shown in their respective regions in the accompanying plot. The plot measures homogenized stiffness as a function of the metric polyhedron, via the mechanical energy (per unit cell) required to achieve a strain of $\epsilon = 0.01$ along the horizontal axis in a periodic sample.

3D cellular metamaterials are valued for many unique and useful mechanical properties. They enable lightweight, high-strength structures, with a wide range of directional stiffness profiles and possible auxetic behaviour. Infill patterns based on triply-periodic minimal surfaces (TPMS) are commonly used in additive manufacturing due to their high strength-to-weight ratio and near-isotropic mechanical behaviour. While existing work provides a wide range of cellular metamaterials to choose from, optimization of these patterns remains a significant challenge due to the diverse space of possible surface topologies and the lack of a unified parameterization. As a promising alternative, Voronoi diagrams with star-shaped distance metrics have been shown to provide a continuous parameterization of 2D cellular metamaterials, opening a rich space of possible designs. Extending the work of [Zhou et al. 2025], we provide a novel, differentiable construction of 3D volumetric Voronoi diagrams with star-shaped metrics. We integrate our formulation into a complete pipeline for mechanical metamaterial optimization, demonstrating the flexibility of star-shaped metric Voronoi diagrams to create periodic structures with a diverse range of directional stiffness profiles and

stress-strain curves. Furthermore, we demonstrate the applicability of this framework to heterogeneous, smoothly graded cellular structures.

CCS Concepts: • **Computing methodologies** → **Shape modeling; Physical simulation.**

Additional Key Words and Phrases: Metamaterial, Voronoi Diagram, Differentiable Simulation, Discrete Shell, Topology Optimization

ACM Reference Format:

Logan Numerow, Stelian Coros, and Bernhard Thomaszewski. 2025. Star-Shaped Distance Voronoi Diagrams for 3D Metamaterial Design. In *SIGGRAPH Asia 2025 Conference Papers (SA Conference Papers '25)*, December 15–18, 2025, Hong Kong, Hong Kong. ACM, New York, NY, USA, 10 pages. <https://doi.org/10.1145/3757377.3763996>

1 Introduction

From structural materials and biomedical scaffolds to acoustic insulation and heat exchange, 3D cellular metamaterials combine material properties and geometry to achieve unique combinations of physical properties. Among existing structures, triply periodic minimal surfaces (TPMS) stand out for their smooth topology, high symmetry and efficient material distribution [Schoen 1970]. While these periodic patterns offer predictable performance and ease of fabrication, the overall design space remains constrained by the limited number of known surface families. This fact restricts the achievable range of stiffness, anisotropy or Poisson's ratio, particularly when subject to constraints on volume fraction. As such, there

Authors' Contact Information: Logan Numerow, ETH Zürich, Zürich, Switzerland, logan.numerow@inf.ethz.ch; Stelian Coros, ETH Zürich, Zürich, Switzerland, scoros@inf.ethz.ch; Bernhard Thomaszewski, ETH Zürich, Zürich, Switzerland, bthomasz@ethz.ch.



This work is licensed under a Creative Commons Attribution 4.0 International License. *SA Conference Papers '25, Hong Kong, Hong Kong*
© 2025 Copyright held by the owner/author(s).
ACM ISBN 979-8-4007-2137-3/2025/12
<https://doi.org/10.1145/3757377.3763996>

is a growing body of research devoted to the development of new 3D metamaterial architectures for targeted mechanical properties.

The space of patterns induced by Voronoi diagrams is more flexible in these regards. Given a set of *sites*, the Voronoi diagram is defined as the set of points that are equidistant from their closest-sites, which in 3D forms the structure of a closed-cell foam. Chew and Dyrsdale [1985] expand the space of Voronoi diagrams through the exploration of generalized distance functions with convex level sets. Martínez et al. [2019] introduce generalizations to non-convex star-shaped level sets, massively enriching the space of possible cell shapes. They explore the range of mechanical properties for 2D structured sheet materials achievable within this parameterization, including auxetic materials with negative Poisson’s ratio. Zhou et al. [2025] present a closed-form differentiable construction of star-shaped distance Voronoi diagrams in 2D and on surfaces.

In this work, we present a closed-form construction of 3D volumetric star-shaped distance Voronoi diagrams, further extending the work of Martínez et al. [2019], Efremov et al. [2021], and Zhou et al. [2025]. Relative to the 2D and surface-bound constructions presented by Zhou et al. [2025], our 3D volumetric construction involves a new and much larger set of vertex and edge types, and requires more complex logic to determine edge geometry during the construction process.

We use star-shaped distance Voronoi diagrams to parameterize a family of cellular metamaterials. Our novel method for selective exclusion of Voronoi diagram faces expands the design space from closed-cell foam structures to include porous topologies typical of TPMS and other popular metamaterial geometries. Using a discrete elastic shell simulation framework, we successfully exploit the differentiability of our construction to solve a set of inverse design problems, where we obtain optimized metamaterials matching a range of target mechanical properties. We achieve extremely symmetric as well as highly anisotropic directional stiffness profiles, a variety of nonlinear stress-strain curves, and different types of auxetic behaviour. Finally, we demonstrate the versatility of our parameterization by interpolating between different geometries to achieve smoothly-graded heterogeneous metamaterial structures.

2 Related Work

Metamaterial Design. By precisely tailoring their micro-scale geometry, metamaterials can exhibit a broad spectrum of macromechanical behaviors. The challenge of designing metamaterials with targeted macromechanical properties intersects multiple core areas of computer graphics, such as geometry processing, physics-based simulation, and computational fabrication. As a result, there has been a growing body of work investigating various forms of 2D metasheets [Leimer and Musialski 2020; Li et al. 2022; Martínez et al. 2019; Montes Maestre et al. 2024; Schumacher et al. 2018; Tang et al. 2023] as well as 3D metamaterials [Makatura et al. 2023; Martínez et al. 2016, 2017; Panetta et al. 2017, 2015; Tricard et al. 2020; Zhang et al. 2023]. Machine learning techniques for metamaterial design and characterization have recently also seen increasing interest from the visual computing community [Feng et al. 2024; Li et al. 2023; Xue et al. 2025].

A particular class of methods uses Voronoi diagrams induced by a set of locations and given metrics to generate metamaterials with a wide range of material properties. For example, Martínez leverage procedural Voronoi diagrams with isotropic [2016] and orthotropic [2017] material properties. Closest to our work, Martínez et al. [2019] and Efremov et al. [2021] introduce metamaterials based on generalized Voronoi diagrams with star-shaped metrics. While these works have demonstrated the appeal of using star-shaped metrics for 2D and 3D metamaterial design, they rely on rasterization-based approaches to generate the Voronoi diagrams which define the materials. This rasterization process is inherently discrete, disqualifying it as a basis for gradient-based material design. In this work, we propose a closed-form construction algorithm for 3D Voronoi diagrams induced by star-shaped metrics that is analytically differentiable with respect to site locations and metric parameters. We show that this algorithm is a robust and efficient basis for inverse material design, which we demonstrate by optimizing metamaterials for a diverse set of target behaviors.

Spatially-Varying Metamaterials. Generating structures with spatially varying mechanical properties is a central challenge in metamaterial design. While unit-cell approaches can generate patterns with desired properties [Panetta et al. 2015; Schumacher et al. 2015; Zhu et al. 2017], heterogeneous tessellations can exhibit pattern mismatches or non-smooth transitions at cell boundaries. To avoid these issues, previous work has explored triply-periodic minimal surfaces (TPMS) as a material space that allows for smoothly evolving structures. For example, Hu et al. [2022] optimize global mechanical properties of TPMS-filled geometries via spatial variation of parameters. In this work, we explore a different material space that likewise allows for smoothly-graded structures and, hence, spatially-varying material properties.

Parametric Metamaterials. In recent years, a substantial body of work has emerged in developing parametric metamaterial structures, which can be optimized to achieve specific mechanical properties beyond the range of conventional TPMS. Khaleghi et al. [2021] construct heterogeneous structures, combining families of TPMS in an attempt to interpolate their directional stiffness profiles. Ma et al. [2021] achieve elastic isotropy for homogeneous TPMS geometries by varying surface thickness within the unit cell, a method which has been extended to anisotropic constitutive materials [Zhang et al. 2022]. Xu et al. [2023] generate new families of TPMS-like shells by constructing minimal surfaces between parameterized curves, and Sun et al. [2023] generate piecewise planar periodic shells by reflecting a cubic or tetrahedral sub-cell throughout the unit cube. Other metamaterial families are generated using smoothed distance level sets [Liu et al. 2022] or level sets of heat diffusion [Han et al. 2024] from predefined skeleton structures. Our work presents a highly flexible parameterization of piecewise planar shells. We show that the space of material behavior that can be generated from star-shaped distance Voronoi diagrams is large and diverse, and that our optimization-based approach is an effective tool for navigating this space in an output-oriented way.

Voronoi Diagrams. Due to their continuous parameterization across topology changes, Voronoi diagrams are an attractive

representation of geometry for many applications, including simulation of fluids and foams [Busaryev et al. 2012; de Goes et al. 2015; Hong et al. 2008; Numerow et al. 2024]. Williams et al. [2019] demonstrate the utility of Voronoi diagrams as a compact, implicit and differentiable shape representation—properties which have been exploited for structural design and optimization [Feng et al. 2022; Lumpe et al. 2022; Zhang et al. 2017]. Gradient-based optimization of discrete Voronoi diagram geometry was perhaps first used to generate Centroidal Voronoi tessellations [Liu et al. 2009; Yan et al. 2009, 2011], which have numerous applications in computational sciences, particularly in mesh generation. In this work, we explore the potential of differentiable Voronoi diagrams with generalized metrics for mechanical metamaterial design.

3 Method

To set the stage for our new construction algorithm, we begin with a brief definition of star-shaped distance Voronoi diagrams. We then describe the extension of the closed-form construction algorithm by Zhou et al. [2025] required to produce 3D volumetric Voronoi diagrams. Next, we explain how cellular metamaterials are constructed from these Voronoi diagrams, and how these metamaterials are optimized for desired mechanical properties using simulation and inverse design.

3.1 Star-Shaped Distance Voronoi Diagrams

The Voronoi cell \mathcal{R}_i of a site c_i can be defined as

$$\mathcal{R}_i = \{\mathbf{p} : d_i(\mathbf{p}) < d_j(\mathbf{p}) \ \forall j \neq i\}, \quad (1)$$

where $d_i(\mathbf{p})$ is the distance between point \mathbf{p} and site c_i . Each point in space belongs to the cell corresponding to its closest site. Using non-Euclidean distance measures $d_i(\mathbf{p})$ to determine the Voronoi cell leads to so-called *generalized Voronoi diagrams*.

Following the definition of Martínez et al. [2019] and Zhou et al. [2025], the *star-shaped distance* function about a site c_i is parameterized by a compact star-shaped set $\mathcal{M}_i \subset \mathbb{R}^n$. The set boundary $\partial\mathcal{M}_i$ is analogous to the unit sphere for Euclidean distance; a point $\mathbf{p} \in (c_i + \alpha\partial\mathcal{M}_i)$ has distance $d_i(\mathbf{p}) = \alpha$ to the site. \mathcal{M}_i is *star-shaped* if it contains the origin and fully contains all line segments connecting the origin to $\partial\mathcal{M}_i$.

Polyhedral metric sets \mathcal{M}_i give rise to piecewise linear star-shaped distances. The resulting Voronoi diagrams can be computed in closed form, as has been shown in 2D and on surfaces [Zhou et al. 2025]; in this work, we extend this construction to 3D volumetric Voronoi diagrams.

3.2 Differentiable Construction in 3D

Like the 2D closed-form algorithm by Zhou et al. [2025], our construction takes as input the positions of Voronoi sites c_i , as well as the metric polyhedra \mathcal{M}_i and bounding domain \mathcal{B} given as triangle meshes. The construction uses a partitioning of the space around a site c_i into *cones* (Fig. 2a), where cone \mathcal{K}_i^j corresponds to triangular face \mathcal{F}_j of the metric polyhedron and is the union of all rays extending from c_i through $c_i + \mathcal{F}_j$. The star-shaped distance within cone

\mathcal{K}_i^j is

$$d_i^j(\mathbf{p}) = \frac{\mathbf{n}_i^j \cdot (\mathbf{p} - \mathbf{c}_i)}{b_i^j}, \quad (2)$$

where $\mathbf{n}_i^j \cdot \mathbf{x} + b_i^j = 0$ defines the hyperplane containing \mathcal{F}_i^j . The Voronoi bisector of sites c_0 and c_1 within the intersection of \mathcal{K}_0^j and \mathcal{K}_1^k is the plane

$$\mathcal{K}_0^j \mathcal{K}_1^k = \left\{ \mathbf{x} : \left(b_1^k \mathbf{n}_0^j - b_0^j \mathbf{n}_1^k \right) \cdot \mathbf{x} + \left(b_0^j \mathbf{n}_1^k \cdot \mathbf{c}_1 - b_1^k \mathbf{n}_0^j \cdot \mathbf{c}_0 \right) = 0 \right\}, \quad (3)$$

which follows from requiring equal distance (Eqn. 2) to the two sites.

The geometry of the star-shaped distance Voronoi diagram is defined by *Voronoi vertices* and *Voronoi edges*. Voronoi vertices are intersections of three planes, and Voronoi edges are intersections of two. Each of these planes is either a *boundary plane*, i.e. the plane containing the three vertices of a boundary triangle, or a *Voronoi bisector plane*, i.e. a plane equidistant to two sites within corresponding cones, given by Eqn. 3. The intersection of three planes can be expressed in closed form with respect to the plane equation coefficients, which in turn can be expressed in terms of the algorithm inputs. We can therefore compute the derivatives of Voronoi vertices in closed form, our implementation uses generated code from a computer algebra system.

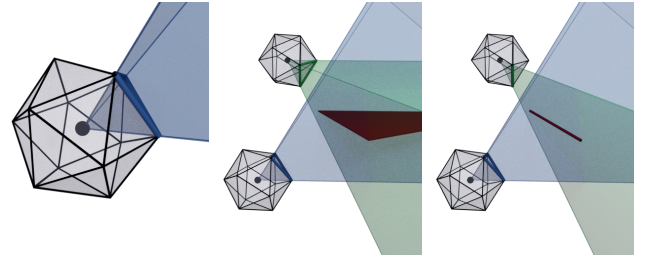


Fig. 2. Illustrations of concepts in the construction of volumetric star-shaped distance Voronoi diagrams. From left to right: (a) A metric cone, i.e. the union of all rays extending from the site through a face of the metric polyhedron. (b) A Voronoi bisector plane (red) between two sites restricted to the intersection of the highlighted cones. This bisector plane is a potential face in the resulting Voronoi diagram. (c) Providing a metric edge (dark green) instead of a face further constrains the bisector to the *cone separator plane* (green), leaving a line segment—the intersection between the previously shown bisector plane and the cone separator plane. This line segment is a potential Voronoi edge of type 1M1V (defined in Table 1).

In 2D, there are five types of Voronoi vertices and two types of edges. This increases in 3D to nine types of vertices and four types of edges. We characterize vertex and edge types in Table 1 by the inputs which specify their geometry. Possible inputs are boundary vertices V_B , edges E_B and faces F_B , as well as metric polyhedron vertices V_C , edges E_C and faces F_C . Boundary vertices, edges, and faces contribute one, two, and three planes respectively to the planes which intersect to form a Voronoi vertex or edge. The number of planes contributed by metric polyhedra is given by $3|V_C| + 2|E_C| + |F_C| - 1$ if the number of metric polyhedron inputs is nonzero, and 0 otherwise, where e.g. $|F_C|$ is the number of metric

polyhedron faces. Fig. 2b illustrates a bisector plane determined by two metric polyhedron faces, and Fig. 2c shows a Voronoi edge determined by a face of one metric polyhedron and an edge of another. For clarification regarding the computation of position for each Voronoi vertex type, see the supplementary material.

Table 1. Types of Voronoi vertices and edges in 3D star-shaped distance Voronoi diagrams. Each row gives the name of the vertex or edge type, as well as the number of each input used to determine its geometry. Possible inputs are boundary vertices V_B , edges E_B and faces F_B , as well as metric polyhedron vertices V_C , edges E_C and faces F_C .

	$ F_B $	$ E_B $	$ V_B $	$ F_C $	$ E_C $	$ V_C $
Vertices						
3B			1			
2B1M		1			1	
2B1V		1		2		
1B1M1V	1			1	1	
1B2V	1			3		
2M1V				1		1
MM1V					2	
1M2V				2	1	
3V				4		
Edges						
2B		1				
1B1V	1			2		
1M1V				1	1	
2V				3		

As in [Zhou et al. 2025], our algorithm builds the Voronoi diagram incrementally by traversing known Voronoi edges. The process is initialized from a vertex of the bounding domain, as these are guaranteed to be present in the final diagram. We maintain a queue of *traces*, each of which indicates a Voronoi edge and the Voronoi vertex at which it originates. For each trace from vertex \mathcal{V} along an edge $e := \mathcal{V} + t\mathbf{d}$, $t > 0$ with direction vector \mathbf{d} , we determine the other endpoint \mathcal{V}' (also a Voronoi vertex) by enumerating possible candidates (see supplementary material) and finding the closest (*i.e.* the endpoint which minimizes t , $t > 0$). After a trace is complete and the opposite endpoint \mathcal{V}' of the edge is determined, if \mathcal{V}' has not yet been added to the Voronoi diagram, new traces starting at \mathcal{V}' are added to the queue. The completion of this process results in a Voronoi edge network; further processing is required to determine the planar Voronoi interfaces. For each bisector $\mathcal{K}_0^j \mathcal{K}_1^k$ present in the final diagram, we collect all edges which share \mathcal{K}_0^j and \mathcal{K}_1^k (or adjacent metric polygon edges) as inputs, project to 2D, and triangulate to obtain interfaces.

For further details, we refer the reader to the supplementary material which, taken together with this section can be used to reproduce the construction algorithm. For a more in-depth description of the tracing process, along with visual examples, see [Zhou et al. 2025].

3.3 Metamaterial Model

In this work, we consider cellular metamaterials constructed from the faces of star-shaped distance Voronoi diagrams. Faces are triangulated, and the result is used as the rest state for a discrete elastic shell simulation, whose degrees of freedom are the positions of mesh vertices. Our simulation model is based on the work of Grinspun et al. [2003], using the StVK model for in-plane tension and compression, along with a hinge-based bending energy model. The stretching energy is

$$U_{\text{stretch}} = k_{\text{stretch}} \bar{A} ((1 - \nu) \text{tr}(\mathbf{E}^2) + \nu \text{tr}(\mathbf{E})^2), \quad (4)$$

where \bar{A} is the undeformed triangle area, \mathbf{E} is the Green strain tensor and ν is Poisson's ratio. The in-plane stiffness k_{stretch} is

$$k_{\text{stretch}} = \frac{Eh}{2(1 - \nu^2)}, \quad (5)$$

where E is Young's modulus and h is the shell thickness. The bending energy, defined per pair of adjacent triangles (*i.e.* per *hinge*), is

$$U_{\text{bend}} = k_{\text{bend}} \frac{3\bar{L}^2}{\bar{\mathcal{A}}} (\theta - \bar{\theta})^2, \quad (6)$$

where \bar{L} is the undeformed length of the shared edge between the two triangles, $\bar{\mathcal{A}}$ is the sum of their undeformed areas, and θ and $\bar{\theta}$ are the deformed and undeformed angles between the triangles. The bending stiffness k_{bend} is

$$k_{\text{bend}} = \frac{Eh^3}{24(1 - \nu^2)}. \quad (7)$$

For the simulations in this work, we use $E = 1.0$ GPa, $\nu = 0.45$ and $h = 0.3$ mm.

3.4 Lattice and Periodicity

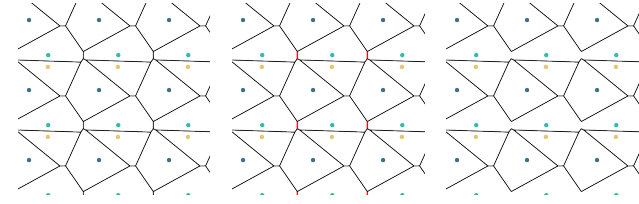
We evaluate the macromechanical properties of our metamaterials using homogenization; we consider an infinite 3D tiling of a periodic structure, and simulate the deformation of a unit cell under periodic boundary conditions.

The bounding domain \mathcal{B} for the construction of the Voronoi diagram is the cube containing a single unit cell. The sites are, however, tiled periodically over a larger volume (*i.e.* $N \times N \times N$ unit cells) such that for large enough N , the Voronoi diagram in the central unit cell will be tileable. This is necessary because a single Voronoi cell can (and usually does, for small numbers of sites per unit cell) span multiple unit cells; sites outside the central unit cell (*i.e.* in nearby unit cells) therefore affect the Voronoi diagram. Sites can be arranged in a regular lattice *e.g.* body-centered or face-centered cubic, or placed arbitrarily within the unit cell. Each site in the unit cell may be assigned an independent metric polyhedron, though corresponding sites in different unit cells must have the same metric polyhedron to obtain periodicity.

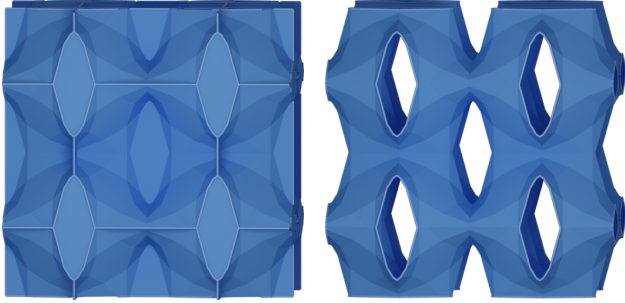
Periodic boundary conditions are enforced by reformulating the simulation degrees of freedom. We add three *lattice vectors* \mathbf{v} as additional degrees of freedom, whose undeformed states are $\bar{\mathbf{v}}_x = [\alpha, 0, 0]^\top$, $\bar{\mathbf{v}}_y = [0, \alpha, 0]^\top$ and $\bar{\mathbf{v}}_z = [0, 0, \alpha]^\top$ for a unit cell with side length α . Subsequently, the degrees of freedom for the position of each vertex \mathcal{V}_{+x} on the $x = \frac{\alpha}{2}$ face of the unit cell are removed; the position of this vertex is computed by adding the lattice vector \mathbf{v}_x

to the position of the corresponding vertex \mathcal{V}_{-x} on the $x = -\frac{\alpha}{2}$ face. The same applies to vertices on the $+y$ and $+z$ faces.

Interface Exclusion. The faces of 3D star-shaped metric Voronoi diagrams, similar to conventional Voronoi diagrams, form closed-cell foam structures. Such patterns have many applications, but are quite stiff by nature, and popular cellular metamaterials including TPMS have porous structures. To obtain open-cell structures, we selectively exclude certain interfaces in the Voronoi diagram. Specifically, we omit faces between corresponding sites in different unit cells as illustrated in Fig. 3. In addition to enabling porosity, this enables our optimization pipeline to adjust the sizes and positions of holes in the structure, adding versatility in terms of mechanical and aesthetic properties.



(a) Illustration of selective interface exclusion in 2D. *Left:* 2D Voronoi diagram constructed from a periodic tiling of sites. Corresponding sites in the tiling have the same color. *Middle:* Interfaces between corresponding sites highlighted in red. *Right:* Highlighted interfaces removed. While this necessarily leads to disconnected geometries in 2D, it often results in porous but fully connected structures in 3D.



(b) A star-shaped distance Voronoi diagram with (left) and without (right) interfaces between corresponding sites in the periodic tiling.

Fig. 3. Selective exclusion of Voronoi interfaces. Rather than being restricted to closed-cell foams, we selectively exclude Voronoi interfaces to achieve more flexible and porous metamaterial structures.

3.5 Metamaterial Design

Directional Stiffness Profiles. The mechanical behaviour of homogenized metamaterials is often characterized by their *directional stiffness profiles*—a measure of resistance to deformation as a function of stretch direction. A 3D example can be found in the work of Khaleghi et al. [2021], where directional stiffness profiles are computed for a range of TPMS-based cellular metamaterials. In this work, we compute mechanical energy $U(\theta, \phi)$ at equilibrium as a function of angle in spherical coordinates θ, ϕ for a constant strain

magnitude ϵ . The equilibrium state is computed for a given angle and strain magnitude by solving an energy minimization problem for the periodic system subject to a directional strain constraint,

$$\mathbf{d}^T F^T F \mathbf{d} = (1 + \epsilon)^2, \quad (8)$$

where $\mathbf{d} = [\sin \theta \cos \phi, \sin \theta \sin \phi, \cos \theta]^T$ is the stretch direction and F is the deformation gradient which satisfies

$$[\mathbf{v}_x \ \mathbf{v}_y \ \mathbf{v}_z] = F[\bar{\mathbf{v}}_x \ \bar{\mathbf{v}}_y \ \bar{\mathbf{v}}_z]. \quad (9)$$

The strain constraint is enforced by adding a penalty term,

$$U_{\text{constraint}} = k_{\text{constraint}} (\mathbf{d}^T F^T F \mathbf{d} - (1 + \epsilon)^2)^2, \quad (10)$$

to the system energy, where $k_{\text{constraint}} = 1e3$ is the penalty weight.

The energy minimization problem, used to find the deformed equilibrium state subject to a given strain direction and magnitude, is solved using Newton's method.

Stress-Strain Curves. Alternatively, we may be interested in the behaviour of a material over a range of strain magnitudes. The relationship between stress and strain for a particular stretch direction is known as the *stress-strain curve*. To compute such curves, we perform stretch tests using the same directional strain constraint (Eqn. 8), but varying the strain magnitude ϵ while holding the stretch direction \mathbf{d} constant. For linearly elastic materials with stress $\sigma = E\epsilon$, the elastic potential energy is proportional to σ^2 , so we approximate the stress-strain curve by computing \sqrt{U} as a function of ϵ .

Inverse Design. We can specify a metamaterial by a set of parameters \mathbf{u} , e.g. Voronoi site positions and/or degrees of freedom of the metric polyhedron. Mechanical properties, e.g. directional stiffness profiles, can be measured as functions of the undeformed state $\mathbf{X}(\mathbf{u})$ and the deformed state $\mathbf{x}(\mathbf{X}(\mathbf{u}))$ of the simulation variables, subject to defined external forces or boundary conditions. Note that the derivatives $\frac{d\mathbf{x}}{d\mathbf{u}}$ of the undeformed geometry are available as described in Section 3.2.

We can optimize for desired mechanical properties by formulating an objective function $L(\mathbf{x}, \mathbf{X}, \mathbf{u})$ and performing equilibrium-constrained optimization,

$$\min_{\mathbf{x}, \mathbf{u}} L(\mathbf{x}, \mathbf{X}(\mathbf{u}), \mathbf{u}) \quad \text{s.t.} \quad \frac{\partial}{\partial \mathbf{x}} U(\mathbf{x}, \mathbf{X}(\mathbf{u})) = \mathbf{0}. \quad (11)$$

The equilibrium state \mathbf{x} which satisfies the constraint is a function of \mathbf{X} and therefore \mathbf{u} , hence the total derivative of L can be calculated as

$$\frac{dL}{d\mathbf{u}} = \frac{\partial L}{\partial \mathbf{x}} \frac{d\mathbf{x}}{d\mathbf{X}} \frac{d\mathbf{X}}{d\mathbf{u}} + \frac{\partial L}{\partial \mathbf{X}} \frac{d\mathbf{X}}{d\mathbf{u}} + \frac{\partial L}{\partial \mathbf{u}}, \quad (12)$$

where the simulation derivatives $\frac{d\mathbf{x}}{d\mathbf{X}}$ are computed using the implicit function theorem,

$$\frac{d}{d\mathbf{X}} \frac{\partial}{\partial \mathbf{x}} U(\mathbf{x}, \mathbf{X}) = \mathbf{0} \rightarrow \frac{d\mathbf{x}}{d\mathbf{X}} = - \left(\frac{\partial^2 U}{\partial \mathbf{x}^2} \right)^{-1} \frac{\partial^2 U}{\partial \mathbf{x} \partial \mathbf{X}}. \quad (13)$$

Recall that finding the deformed equilibrium state $\mathbf{x}(\mathbf{X})$ requires solving a minimization problem, which we achieve using Newton's method. For the equilibrium-constrained optimization of the Voronoi diagram parameters \mathbf{u} , we alternate Gauss-Newton steps and steps using the Globally-Convergent Method of Moving Asymptotes [Svanberg 2002].

Table 2. Results of optimization for target directional stiffness profiles. For each metamaterial, a 2x2x2 tiling of the unit cell is shown, along with a plot comparing its stiffness profile to the target. Target optimization points are shown as black dots in the plot, and the surface representing the stiffness profile is colored according to deviation from the target (as a fraction of the target value). All optimized metamaterials achieve good agreement with their target stiffness profiles.

Target Energy	Initial	Optimized
$\bar{U}_i = 1$		
$\bar{U}_i = \frac{ \mathbf{d}_i }{\max(x_i, y_i, z_i)}$		
$\bar{U}_i r_i = \frac{\bar{U}_i r_i}{\left(1 - \frac{3}{4} e^{-\bar{U}_i^2 z_i^2}\right) \sqrt{1 - \bar{U}_i^2 z_i^2}}$		

3.6 Implementation

Our method is implemented in C++. We use the Eigen library [Guennebaud et al. 2010] for matrix and vector operations, Polyscope [Sharp et al. 2019] for user interface and visualization, and code adapted from WuKong [Li et al. 2024] for discrete elastic shell simulation. Our code can be found at <https://github.com/lnumerow-ethz/StarShapedVoronoi>.

4 Results

We demonstrate the versatility of metamaterials constructed from 3D star-shaped metric Voronoi diagrams, as well as the effectiveness of our optimization pipeline, through a series of inverse design problems. We explore three primary design goals: matching a target shape of the directional stiffness profile for a fixed strain magnitude, matching a target shape of the stress-strain curve for a fixed stretch direction, and achieving auxetic behavior in one or both transverse directions. A final experiment demonstrates the potential for smooth interpolation between metamaterial patterns.

4.1 Stiffness Profile Optimization

We set a target directional stiffness profile by defining a set of optimization points consisting of a direction $\mathbf{d}_i = [x_i, y_i, z_i] = [r_i \cos \theta_i, r_i \sin \theta_i, z_i]$ and target energy \bar{U}_i . In these experiments,

we are interested in the shape of the stiffness profile and not the magnitude, so we define \bar{U}_i only up to a constant factor w . We generate an initial metamaterial using three sites per unit cell and randomly-rotated icosahedra for metric polyhedra, and minimize

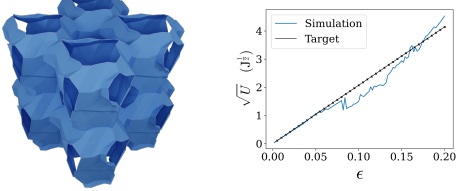
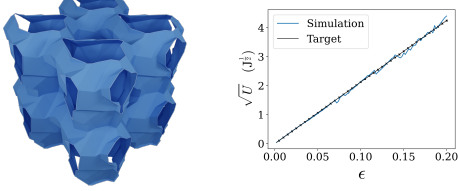
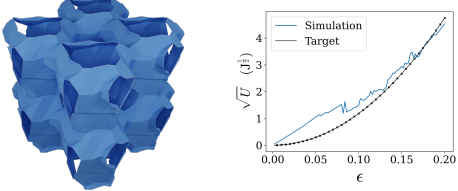
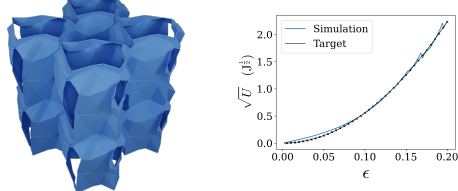
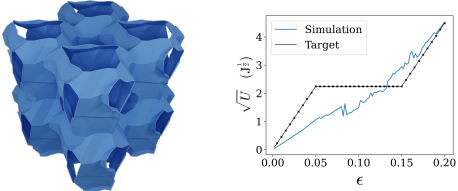
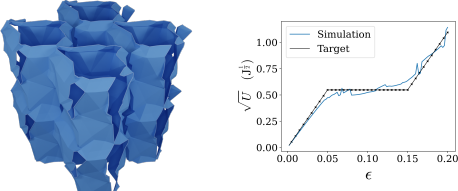
$$L(\mathbf{u}) = \sum_i (U(\mathbf{u}, \mathbf{d}_i) - w\bar{U}_i)^2, \quad (14)$$

with degrees of freedom \mathbf{u} consisting of the cartesian coordinates of sites within the unit cell, Euler angles defining the overall rotation of the metric polyhedron for each site, and the distance of each metric point from the origin. After each optimization iteration, we update w to the value w^* which minimizes L ,

$$w^* = \frac{\sum_i U(\mathbf{d}_i) \bar{U}_i}{\sum_i \bar{U}_i^2}, \quad (15)$$

and continue until convergence or until we cannot make further progress. A fixed strain magnitude of $\epsilon = 0.01$ is used. Table 2 defines the three target stiffness profile shapes by giving \bar{U}_i as a function of \mathbf{d}_i , compares initial and optimized stiffness profiles to the targets, and displays the corresponding metamaterial geometries. The target stiffness profiles are designed by hand and, aside from the isotropic profile (top row), likely not physically feasible. Some mismatch is therefore expected. However, our pipeline achieves a good approximation of the desired stiffness profile in all instances.

Table 3. Results of optimization for target stress-strain curves. For each metamaterial, a 2x2x2 tiling of the unit cell is shown, along with a plot comparing its stress-strain curve to the target. Optimized results achieve good agreement with their targets, with significant deviation only for the third example which asks for constant energy within a wide range of strain.

Target Energy	Initial	Optimized
$\sqrt{\bar{U}_i} = \epsilon_i$		
$\sqrt{\bar{U}_i} = \epsilon_i^2$		
$\sqrt{\bar{U}_i} = \begin{cases} \epsilon_i & \epsilon_i \leq 0.05 \\ 0.05 & 0.05 \leq \epsilon_i \leq 0.15 \\ \epsilon_i - 0.1 & 0.15 \leq \epsilon_i, \end{cases}$		

Similarly, we define optimization points for stress-strain curves by a strain magnitude ϵ_i and target energy \bar{U}_i , again defined up to a constant factor w . We use a fixed stretch direction $\mathbf{d} = [1, 0, 0]$ and strain magnitude ranging from 0 to 0.2. The initial metamaterial is generated using two sites per unit cell and once-subdivided octahedral metric polyhedra (18 vertices). Degrees of freedom are as for the directional stiffness profile examples. The objective function is

$$L(\mathbf{u}) = \sum_i \frac{1}{\epsilon_i^4} (U(\mathbf{u}, \epsilon_i) - w\bar{U}_i)^2. \quad (16)$$

Due to the weight of terms in the summation, the w update between steps becomes

$$w^* = \frac{\sum_i \frac{1}{\epsilon_i^4} U(\epsilon_i) \bar{U}_i}{\sum_i \frac{1}{\epsilon_i^4} \bar{U}_i^2}. \quad (17)$$

Table 3 defines the three target stress-strain curve shapes and shows the results of these experiments. The results match the targets closely, with noticeable error only for the piecewise linear target shown in row 3. It is worth noting that asking for constant \bar{U} for a wide range of ϵ is equivalent to a zero-stiffness behavior, which can only be achieved through buckling and other nonlinear effects [Frenzel et al. 2016; Huang et al. 2024].

4.2 Auxetic Metamaterials

In an additional set of inverse design experiments, we optimize metamaterials to exhibit auxetic behaviour. Specifically, we stretch the metamaterial along the x -axis $\mathbf{d} = \hat{\mathbf{x}} = [1, 0, 0]$ with strain $\epsilon_x = 0.01$ and optimize for positive transverse strains ϵ_y and ϵ_z . The objective functions for the two experiments are

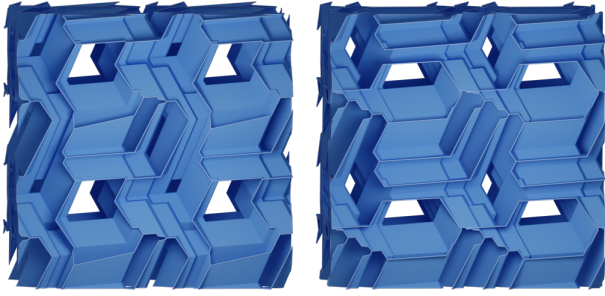
$$L_1 = (\bar{\mathbf{y}}^T F^T F \bar{\mathbf{y}} - (1 + \epsilon_x))^2, \quad (18)$$

$$L_2 = (\bar{\mathbf{y}}^T F^T F \bar{\mathbf{y}} - (1 + \epsilon_x))^2 + (\bar{\mathbf{z}}^T F^T F \bar{\mathbf{z}} - (1 + \epsilon_x))^2, \quad (19)$$

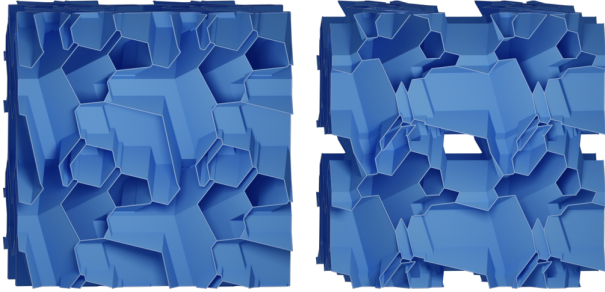
which encourage $\epsilon_y = \epsilon_x$ and $\epsilon_y = \epsilon_z = \epsilon_x$ respectively. The degrees of freedom for these experiments are the same as in section 4.1. The initial metamaterial for each case uses four sites per unit cell and randomly-rotated tetrahedral metric polyhedra. Fig. 4 shows the initial and optimized geometry for each experiment and indicates the strain in each transverse direction when subject to a fixed strain in the x -direction. When optimizing for positive ϵ_y only, we achieve Poisson's ratio $\nu_{xy} = -\epsilon_y/\epsilon_x = -0.95$, and when optimizing for both transverse strains we achieve $\nu_{xy} = -\epsilon_y/\epsilon_x = -0.70$ and $\nu_{xz} = -\epsilon_z/\epsilon_x = -0.71$.

4.3 Directional Young's Modulus

As a validation of our objective formulation for achieving directional stiffness profiles, we compare to the directional Young's modulus defined by Schumacher et al. [2018]. Table 4 shows both measures



(a) Optimizing for expansion in y subject to stretching in the x -direction (objective L_1). *Left:* Initial metamaterial with $\epsilon_x = 0.01$, $\epsilon_y = -0.0001$, $\epsilon_z = -0.0049$. *Right:* Optimized metamaterial with $\epsilon_x = 0.01$, $\epsilon_y = 0.0095$, $\epsilon_z = -0.048$.



(b) Optimizing for expansion in both y and z subject to stretching in the x -direction (objective L_2). *Left:* Initial metamaterial with $\epsilon_x = 0.01$, $\epsilon_y = -0.0033$, $\epsilon_z = -0.0021$. *Right:* Optimized metamaterial with $\epsilon_x = 0.01$, $\epsilon_y = 0.0070$, $\epsilon_z = 0.0071$.

Fig. 4. Results of metamaterial optimization for auxetic behaviour in one (a) and both (b) transverse directions.

computed for the initial and optimized metamaterials in Table 2. Although we observe a clear correlation between the two measures, the differences illustrate a need for further investigation to determine the best objective formulation to achieve the desired mechanical behaviour. For details regarding the computation of directional Young's modulus, we refer the reader to the supplementary material.

4.4 Metric Interpolation

Finally, to demonstrate the ability of our method to smoothly interpolate between metamaterial patterns, we construct a star-shaped distance Voronoi diagram in an elongated domain with sites arranged in a body-centered cubic (BCC) lattice. We choose three metric polyhedra \mathcal{M}_1 , \mathcal{M}_2 and \mathcal{M}_3 ; the first one is a regular icosahedron, whereas the other two are perturbed icosahedra obtained by scaling the distance of each vertex from the origin ρ by a random value between 0.4 and 1.6. We assign a metric polyhedron to a site depending on its x -coordinate

$$\mathcal{M}_i = \begin{cases} \mathcal{M}_1 & x_i \leq -4 \\ \mathcal{M}_2 & -0.5 \leq x_i \leq 0.5 \\ \mathcal{M}_3 & 4 \leq x_i, \end{cases} \quad (20)$$

Table 4. Comparison between our directional stiffness profile (using total mechanical energy) and the directional Young's modulus defined by Schumacher et al. [2018] for the four metamaterials shown in Table 2. Though we observe a clear correlation between the two measures, there are notable differences, including additional asymmetries in the directional Young's modulus. Further investigation is required to determine the best objective formulation to achieve the desired mechanical behaviour.

Mechanical Energy	Directional Young's Modulus

linearly interpolating between them outside these ranges. Fig. 1 shows the resulting metamaterial, where we observe visually smooth transitions between the resulting patterns. Unfortunately, it is unclear how to determine the effective stiffness distribution in such an interpolated material. For reference, we instead plot the stiffness of the homogenized interpolated metamaterials in terms of $U(\vec{x}, \epsilon = 0.01)$. It can be seen that, despite the smoothness of the interpolated pattern, the point-wise stiffness of the corresponding homogenized material may vary substantially.

5 Conclusions

We extended the algorithm of Zhou et al. [2025] to enable the construction of 3D volumetric star-shaped distance Voronoi diagrams, and integrated this into a framework which generates optimized cellular metamaterials using gradient-based inverse design. We demonstrated the versatility of our design space by optimizing for 3D directional stiffness profiles ranging from highly orthotropic to almost perfectly isotropic, in addition to diverse stress-strain curves along a single stretch direction.

5.1 Limitations & Future Work

While this paper focuses exclusively on so-called *shellular* metamaterials constructed from the faces of Voronoi diagrams, we could further consider e.g. elastic rod networks constructed from Voronoi edges, or combinations of the two. This would greatly enrich the space of metamaterials that can be achieved using our paradigm.

As indicated by the results of Section 4.3, we should consider alternative formulations for optimization objectives which may better align with typical design goals. Furthermore, there is a much wider range of useful optimization objectives to be explored, including objectives such as strength-to-weight ratio which encourage reducing the amount of material used. Linearly interpolating between metric polyhedra did not achieve corresponding grading of mechanical properties, though we believe that this could be achieved through optimization.

Future work should involve testing on physical prototypes to compare with state-of-the-art infills. This would require thickening the geometry to achieve printable 3D models, and possibly chamfering along edges to better distribute internal forces. Our framework could then be used to develop a collection of optimized infill patterns with a range of useful mechanical properties.

Acknowledgments

We are grateful to the anonymous reviewers for their valuable feedback. This work was supported by the Swiss National Science Foundation through SNF project grant 200021_200644.

References

- Oleksiy Busaryev, Tamal K. Dey, Huamin Wang, and Zhong Ren. 2012. Animating Bubble Interactions in a Liquid Foam. *ACM Trans. Graph.* 31, 4, Article 63 (jul 2012), 8 pages. doi:10.1145/2185520.2185559
- L. Paul Chew and Robert L. (Scott) Dyrsdale. 1985. Voronoi diagrams based on convex distance functions. In *Proceedings of the First Annual Symposium on Computational Geometry* (Baltimore, Maryland, USA) (SCG '85). Association for Computing Machinery, New York, NY, USA, 235–244. doi:10.1145/323233.323264
- Fernando de Goes, Corentin Wallez, Jin Huang, Dmitry Pavlov, and Mathieu Desbrun. 2015. Power Particles: An Incompressible Fluid Solver Based on Power Diagrams. *ACM Trans. Graph.* 34, 4, Article 50 (jul 2015), 11 pages. doi:10.1145/2766901
- Semyon Efremov, Jonàs Martínez, and Sylvain Lefebvre. 2021. 3D periodic cellular materials with tailored symmetry and implicit grading. *Computer-Aided Design* 140 (2021), 103086.
- Fan Feng, Shiyong Xiong, Ziyue Liu, Zangyueyang Xian, Yuqing Zhou, Hiroki Kobayashi, Atsushi Kawamoto, Tsuyoshi Nomura, and Bo Zhu. 2022. Cellular topology optimization on differentiable Voronoi diagrams. *Internat. J. Numer. Methods Engrg.* 124, 1 (sep 2022), 282–304. doi:10.1002/nme.7121
- Xudong Feng, Huamin Wang, Yin Yang, and Weiwei Xu. 2024. Neural-Assisted Homogenization of Yarn-Level Cloth. In *ACM SIGGRAPH 2024 Conference Papers* (Denver, CO, USA) (SIGGRAPH '24). Association for Computing Machinery, New York, NY, USA, Article 80, 10 pages. doi:10.1145/3641519.3657411
- Tobias Frenzel, Claudio Findeisen, Mumer Kadac, Peter Gumbsch, and Martin Wegener. 2016. Tailored Buckling Microlattices as Reusable Light-Weight Shock Absorbers. *Advanced materials (Deerfield Beach, Fla.)* 28, 28 (2016), 5865–5870.
- Eitan Grinspun, Anil N. Hirani, Mathieu Desbrun, and Peter Schröder. 2003. Discrete shells. In *Proceedings of the 2003 ACM SIGGRAPH/Eurographics Symposium on Computer Animation* (San Diego, California) (SCA '03). Eurographics Association, Goslar, DEU, 62–67.
- Gaël Guennebaud, Benoît Jacob, et al. 2010. Eigen v3. <http://eigen.tuxfamily.org>.
- Jiacheng Han, Xiaoya Zhai, Lili Wang, Di Zhang, Junhao Ding, Winston Wai Shing Ma, Xu Song, Wei-Hsin Liao, Ligang Liu, Jun Wu, and Xiao-Ming Fu. 2024. Inverse-designed 3D sequential metamaterials achieving extreme stiffness. *Materials & Design* 247 (2024), 113350. doi:10.1016/j.matdes.2024.113350
- Jeong-Mo Hong, Ho-Young Lee, Jong-Chul Yoon, and Chang-Hun Kim. 2008. Bubbles alive. *ACM Trans. Graph.* 27, 3 (aug 2008), 1–4. doi:10.1145/1360612.1360647
- Jiangbei Hu, Shengfa Wang, Baojun Li, Fengqi Li, Zhongxuan Luo, and Ligang Liu. 2022. Efficient Representation and Optimization for TPMS-Based Porous Structures. *IEEE Transactions on Visualization and Computer Graphics* 28, 7 (2022), 2615–2627. doi:10.1109/TVCG.2020.3037697
- Zizhou Huang, Daniele Panozzo, and Denis Zorin. 2024. Optimized shock-protecting microstructures. *ACM Trans. Graph.* 43, 6, Article 181 (Nov. 2024), 21 pages. doi:10.1145/3687765
- Saeed Khaleghi, Fayyaz N. Dehnavi, Mostafa Baghani, Masoud Safdari, Kui Wang, and Majid Baniassadi. 2021. On the directional elastic modulus of the TPMS structures and a novel hybridization method to control anisotropy. *Materials & Design* 210 (2021), 110074. doi:10.1016/j.matdes.2021.110074
- Kurt Leimer and Przemysław Musiałski. 2020. Reduced-Order Simulation of Flexible Meta-Materials. *Proceedings - SCF 2020: ACM Symposium on Computational Fabrication*. doi:10.1145/3424630.3425411
- Yue Li et al. 2024. WuKong. <https://github.com/liyuesolo/Wukong2024>.
- Yue Li, Stelian Coros, and Bernhard Thomaszewski. 2023. Neural Metamaterial Networks for Nonlinear Material Design. *ACM Trans. Graph.* 42, 6, Article 186 (dec 2023), 13 pages. doi:10.1145/3618325
- Yue Li, Juan Montes, Bernhard Thomaszewski, and Stelian Coros. 2022. Programmable Digital Weaves. *IEEE Robotics and Automation Letters* 7, 2 (2022), 2891–2896.
- Peiqing Liu, Bingteng Sun, Jikai Liu, and Lin Lu. 2022. Parametric shell lattice with tailored mechanical properties. *Additive Manufacturing* 60 (2022), 103258. doi:10.1016/j.addma.2022.103258
- Yang Liu, Wenping Wang, Bruno Lévy, Feng Sun, Dong-Ming Yan, Lin Lu, and Chenglei Yang. 2009. On Centroidal Voronoi Tessellation—Energy Smoothness and Fast Computation. *ACM Trans. Graph.* 28, 4, Article 101 (sep 2009), 17 pages. doi:10.1145/1559755.1559758
- Thomas S Lumpe, Michael Tao, Kristina Shea, and David I W Levin. 2022. Computational design and fabrication of active 3D-printed multi-state structures for shape morphing. *Smart Materials and Structures* 32, 1 (dec 2022), 015008. doi:10.1088/1361-665X/aca5d6
- Qingping Ma, Lei Zhang, Junhao Ding, Shuo Qu, Jin Fu, Mingdong Zhou, Ming Wang Fu, Xu Song, and Michael Yu Wang. 2021. Elastically-isotropic open-cell minimal surface shell lattices with superior stiffness via variable thickness design. *Additive Manufacturing* 47 (2021), 102293. doi:10.1016/j.addma.2021.102293
- Liane Makatura, Bohan Wang, Yi-Lu Chen, Bolei Deng, Chris Wojtan, Bernd Bickel, and Wojciech Matusik. 2023. Procedural Metamaterials: A Unified Procedural Graph for Metamaterial Design. 42, 5, Article 168 (jul 2023), 19 pages. doi:10.1145/3605389
- Jonàs Martínez, Jérémie Dumas, and Sylvain Lefebvre. 2016. Procedural voronoi foams for additive manufacturing. *ACM Transactions on Graphics (TOG)* 35, 4 (2016), 1–12.
- Jonàs Martínez, Mélina Skouras, Christian Schumacher, Samuel Hornus, Sylvain Lefebvre, and Bernhard Thomaszewski. 2019. Star-shaped metrics for mechanical metamaterial design. *ACM Transactions on Graphics (TOG)* 38, 4 (2019), 1–13.
- Jonàs Martínez, Haichuan Song, Jérémie Dumas, and Sylvain Lefebvre. 2017. Orthotropic k-nearest foams for additive manufacturing. *ACM Transactions on Graphics (TOG)* 36, 4 (2017), 1–12.
- Juan Sebastian Montes Maestre, Yinwei Du, Ronan Hinchet, Stelian Coros, and Bernhard Thomaszewski. 2024. FlexScale: Modeling and Characterization of Flexible Scaled Sheets. *ACM Trans. Graph.* 43, 4, Article 86 (July 2024), 14 pages. doi:10.1145/3658175
- Logan Numerow, Yue Li, Stelian Coros, and Bernhard Thomaszewski. 2024. Differentiable Voronoi Diagrams for Simulation of Cell-Based Mechanical Systems. *ACM Trans. Graph.* 43, 4, Article 69 (July 2024), 11 pages. doi:10.1145/3658152
- Julian Panetta, Abtin Rahimian, and Denis Zorin. 2017. Worst-case stress relief for microstructures. *ACM Transactions on Graphics (TOG)* 36, 4 (2017), 1–16.
- Julian Panetta, Qingnan Zhou, Luigi Malomo, Nico Pietroni, Paolo Cignoni, and Denis Zorin. 2015. Elastic textures for additive fabrication. *ACM Transactions on Graphics (TOG)* 34, 4 (2015), 1–12.
- Alan H. Schoen. 1970. *Infinite Periodic Minimal Surfaces Without Self-Intersections*. Technical Report NASA Technical Note D-5541. NASA Electronics Research Center, Cambridge, MA, USA. <https://ntrs.nasa.gov/citations/19700020472>
- Christian Schumacher, Bernd Bickel, Jan Rys, Steve Marschner, Chiara Daraio, and Markus Gross. 2015. Microstructures to control elasticity in 3D printing. *ACM Trans. Graph.* 34, 4, Article 136 (July 2015), 13 pages. doi:10.1145/2766926
- Christian Schumacher, Steve Marschner, Markus Gross, and Bernhard Thomaszewski. 2018. Mechanical characterization of structured sheet materials. *ACM Transactions*

- on *Graphics (TOG)* 37, 4 (2018), 1–15.
- Nicholas Sharp et al. 2019. Polyscope. www.polyscope.run.
- Bingteng Sun, Xin Yan, Peiqing Liu, Yang Xia, and Lin Lu. 2023. Parametric plate lattices: Modeling and optimization of plate lattices with superior mechanical properties. *Additive Manufacturing* 72 (2023), 103626. doi:10.1016/j.addma.2023.103626
- Krister Svanberg. 2002. A Class of Globally Convergent Optimization Methods Based on Conservative Convex Separable Approximations. *SIAM Journal on Optimization* 12, 2 (2002), 555–573. doi:10.1137/S1052623499362822
- Pengbin Tang, Stelian Coros, and Bernhard Thomaszewski. 2023. Beyond Chainmail: Computational Modeling of Discrete Interlocking Materials. *ACM Trans. Graph.* 42, 4, Article 84 (jul 2023), 12 pages. doi:10.1145/3592112
- Thibault Tricard, Vincent Tavernier, Cédric Zanni, Jonàs Martínez, Pierre-Alexandre Hugron, Fabrice Neyret, and Sylvain Lefebvre. 2020. Freely orientable microstructures for designing deformable 3D prints. *ACM Trans. Graph.* 39, 6 (2020), 211–1.
- Francis Williams, Daniele Panozzo, Kwang Moo Yi, and Andrea Tagliasacchi. 2019. VoronoiNet: General Functional Approximators with Local Support. *2020 IEEE/CVF Conference on Computer Vision and Pattern Recognition Workshops (CVPRW)* (2019), 1069–1073. <https://api.semanticscholar.org/CorpusID:208910620>
- Yonglai Xu, Hao Pan, Ruonan Wang, Qiang Du, and Lin Lu. 2023. New families of triply periodic minimal surface-like shell lattices. *Additive Manufacturing* 77 (2023), 103779. doi:10.1016/j.addma.2023.103779
- Tianyang Xue, Haochen Li, Longdu Liu, Paul Henderson, Pengbin Tang, Lin Lu, Jikai Liu, Haisen Zhao, Hao Peng, and Bernd Bickel. 2025. MIND: Microstructure INverse Design with Generative Hybrid Neural Representation. arXiv:2502.02607 [cs.CV] <https://arxiv.org/abs/2502.02607>
- Dong-Ming Yan, Bruno Levy, Yang Liu, Feng Sun, and Wenping Wang. 2009. Isotropic Remeshing with Fast and Exact Computation of Restricted Voronoi Diagram. *Comput. Graph. Forum* 28 (07 2009), 1445–1454. doi:10.1111/j.1467-8659.2009.01521.x
- Dong-Ming Yan, Wenping Wang, Bruno Levy, and Yang Liu. 2011. Efficient Computation of Clipped Voronoi Diagram for Mesh Generation. *Computer-Aided Design* 45 (09 2011). doi:10.1016/j.cad.2011.09.004
- Lei Zhang, Qingping Ma, Junhao Ding, Shuo Qu, Jin Fu, Ming Wang Fu, Xu Song, and Michael Yu Wang. 2022. Design of elastically isotropic shell lattices from anisotropic constitutive materials for additive manufacturing. *Additive Manufacturing* 59 (2022), 103185. doi:10.1016/j.addma.2022.103185
- Xiaoting Zhang, Guoxin Fang, Chengkai Dai, Jouke Verlinden, Jun Wu, Emily Whiting, and Charlie C.L. Wang. 2017. Thermal-Comfort Design of Personalized Casts. In *Proceedings of the 30th Annual ACM Symposium on User Interface Software and Technology* (Québec City, QC, Canada) (*UIST '17*). Association for Computing Machinery, New York, NY, USA, 243–254. doi:10.1145/3126594.3126600
- Zhan Zhang, Christopher Brandt, Jean Jouve, Yue Wang, Tian Chen, Mark Pauly, and Julian Panetta. 2023. Computational Design of Flexible Planar Microstructures. *ACM Trans. Graph.* 42, 6, Article 185 (dec 2023), 16 pages. doi:10.1145/3618396
- Haoyang Zhou, Logan Numerow, Stelian Coros, and Bernhard Thomaszewski. 2025. Closed-Form Construction of Voronoi Diagrams with Star-Shaped Metrics. *ACM Transactions on Graphics (TOG)* 44, 6 (2025).
- Bo Zhu, Mélina Skouras, Desai Chen, and Wojciech Matusik. 2017. Two-scale topology optimization with microstructures. *ACM Transactions on Graphics (TOG)* 36, 4 (2017), 1.